Available online at www.sciencedirect.com
ScienceDirect
Journal of Computational Physics 225 (2007) 2377–2397
JOURNAL OF COMPUTATIONAL PHYSICS
www.elsevier.com/locate/jcp

Finite difference approximations of first derivatives for three-dimensional grid singularities

Herwig A. Grogger *

University of Applied Sciences FH Joanneum, Alte Poststrasse 149, A-8010 Graz, Austria

Received 25 August 2006; received in revised form 30 January 2007; accepted 22 March 2007
Available online 11 April 2007

Abstract

Explicit finite difference approximations of first derivatives are developed for three-dimensional four-block and six-block grid singularities. The schemes for the four-block singularity are of second, fourth and sixth order of accuracy, whereas the six-block schemes are of second and fourth order. The work extends a recently reported idea of developing schemes for two-dimensional grid singularities to three dimensions.

Term matching of Taylor-series expansions of the dependent variable at neighboring points and the requirement for non-dissipative schemes do not provide enough equations to determine all coefficients; the open coefficients are determined through an optimization process to minimize the isotropy error of the numerical phase velocity. Owing to that optimization, the phase velocities and time-step limits for explicit time integration are very isotropic. The spectral characteristics, as dispersion and dissipation property and the time-step limit indicate that the proposed schemes for grid singularities can be well combined with Cartesian schemes of the same order of accuracy on the regular part of a computational mesh.

The formal orders of accuracy of the proposed schemes are verified using the three-dimensional linear convection equation. Stability limits for explicit time integration are given.

Keywords: Finite difference; Grid singularity; Linear wave propagation; Isotropy error; Numerical stability

1. Introduction

Recently, finite difference approximations of first derivatives for two-dimensional grid singularities have been proposed [1]. The coefficients multiplying the dependent variable at the point locations are chosen such that the resulting finite difference approximations are non-dissipative and their numerical phase velocities exhibit minimized isotropy error. Further characteristics of those finite differences are time-step limits, which are greater than those of central differences of the same order of accuracy. Consequently, they are well suited to be used at grid singularities, i.e. at points, where a regular (Cartesian) differencing stencil cannot be established.

DOI of original article: 10.1016/j.jcp.2006.01.017.
* Tel.: +43 316 5453 8457; fax: +43 316 5453 8401.
E-mail address: herwig.grogger@fh-joanneum.at

0021-9991/$ - see front matter
doi:10.1016/j.jcp.2007.03.027

The current work extends that idea to three dimensions. As in two dimensions, equations to determine the coefficients are obtained by term matching of Taylor-series expansions and the requirement for non-dissipative schemes. Still, there remain undetermined coefficients, which are found by minimizing the isotropy error. In that way, finite difference approximations of first derivatives for three-dimensional four-block and six-block singularities are obtained. The proposed schemes increase the flexibility of treating three-dimensional computational meshes with grid singularities, which is an inherent drawback of regular finite difference approximations.

Few works on finite difference approximations for three-dimensional grids have been reported. Usually, one-dimensional approximations are applied along each grid line, regardless of the dimension of a computational grid. A possible non-orthogonality is taken into account by coordinate transformation. Emphasis on isotropy of two- and three-dimensional finite differences is given in a work by Kumar [2], where diagonal points are involved in the differencing stencils to increase the isotropy of approximations of first and second derivatives in the context of solidification simulations. Nevertheless, these finite differences are based on regular i, j, k-addressing.

A different approach to increase isotropy is followed by Wagner and Schneider [3]. A weighted linear combination of second order finite differences based on different stencils is used, and the weights are chosen such that the resulting scheme is fourth order accurate in terms of isotropy. But again, the differencing stencils are based on regular grids.

Theoretically, a meshless approach similar to that by Chung [4] was possible to develop finite differences for three-dimensional grid singularities. Here, exactly the same number of points are involved in the finite difference, which are necessary to fulfill a certain order of accuracy. As a result, the approximation might be dissipative, which could lead to numerical instability in hyperbolic problems.

Optimization of finite differences has been performed with different objectives. For example, in acoustic wave propagation or large eddy simulation of flows (LES), dispersion of explicit schemes has been minimized by reducing the formal order of accuracy of the scheme and using the undetermined coefficient in the optimization process [5,6]. Similar approaches have also been performed for implicit, or compact, finite differences [7–9]. A recent survey article on high order methods has been presented by Ekaterinaris [10], where, amongst others, several optimized finite difference schemes are reviewed.

In contrast to regular finite differences, there are more points present in the differencing stencils for singular points than which are necessary to fulfill a certain order of accuracy; though they are too few in number to fulfill the next higher order. Those coefficients do not contribute to the order of the scheme; they are subjected to an optimization process to minimize anisotropy.

The current work is organized as follows: Section 2 reviews Fourier-analysis of hyperbolic equations. In Section 3 the determining equations of the coefficients are discussed. Sections 4 and 5 present finite differences for three-dimensional four-block and six-block singularities, respectively. In Section 6 the stability of the proposed schemes is investigated based on the three-dimensional linear convection equation and explicit time integration. Numerical experiments in Section 7 comprise the evaluation of the formal order of accuracy using the three-dimensional linear convection equation, and scattering of sound by a plane wall governed by the linearized Euler equations. The proposed schemes are discussed in Section 8, and a summary and conclusion closes the paper.

2. Fourier analysis of discretizations for linear wave propagation

This section presents a short overview of Fourier analysis of discretizations of three-dimensional wave propagation, and is included to clarify terminology. Notation follows that of [1]. A comprehensive description of Fourier analysis of discretization errors of hyperbolic equations can be found in [11].

To analyse the isotropy of finite differences of first derivatives in three dimensions, the corresponding linear convection equation is employed,

$$U = U(\vec{x}, t) : \frac{\partial U}{\partial t} + \vec{c} \cdot \nabla U = 0, \tag{1}$$

with c denoting the velocity vector of wave propagation,

$$\vec{c} = \begin{pmatrix} c_x \\ c_y \\ c_z \end{pmatrix} = c \begin{pmatrix} \sin\vartheta\cos\varphi \\ \sin\vartheta\sin\varphi \\ \cos\vartheta \end{pmatrix}. \tag{2}$$

Here, c is the propagation speed, ϑ denotes the angle between the positive z-axis and the position vector $\vec{x}$, and φ is the angle between the positive x-axis and $\vec{x}$. For the analysis of discretizations, long-hand Cartesian notation of (1) may be more convenient,

$$\frac{\partial U}{\partial t} + c\left(\sin\vartheta\cos\varphi\frac{\partial U}{\partial x} + \sin\vartheta\sin\varphi\frac{\partial U}{\partial y} + \cos\vartheta\frac{\partial U}{\partial z}\right) = 0. \tag{3}$$

Approximating spatial derivatives at position i by finite differences involving N neighboring points,

$$\left.\frac{\partial U}{\partial x}\right|_i \approx \frac{1}{L}\sum_{j=0}^{N} a_{x,j}u_{i+j}, \quad \left.\frac{\partial U}{\partial y}\right|_i \approx \frac{1}{L}\sum_{j=0}^{N} a_{y,j}u_{i+j}, \quad \text{and} \quad \left.\frac{\partial U}{\partial z}\right|_i \approx \frac{1}{L}\sum_{j=0}^{N} a_{z,j}u_{i+j}, \tag{4}$$

with u_i denoting the approximation of U at position i, and L being the point-to-point distance, gives the semi-discretized version of (1),

$$\frac{\mathrm{d}u_i}{\mathrm{d}t} = -\frac{c}{L}\left(\sin\vartheta\cos\varphi\sum_{j=0}^{N} a_{x,j}u_{i+j} + \sin\vartheta\sin\varphi\sum_{j=0}^{N} a_{y,j}u_{i+j} + \cos\vartheta\sum_{j=0}^{N} a_{z,j}u_{i+j}\right), \tag{5}$$

for the discrete variable $u_i(t)$. Space Fourier transformation allows to evaluate the spectral characteristics of the spatial approximation,

$$\frac{\mathrm{d}\hat{u}}{\mathrm{d}t} = H(k,\vartheta,\varphi)\hat{u}, \tag{6}$$

with $\hat{u}$ denoting the discrete Fourier transform of u_i, $H(k,\vartheta,\varphi)$ is the spectral function of the spatial approximation, and k stands for the wave-number, i.e. the spatial frequency. The real part of H can be related to the dissipative characteristics of the discretization, whereas the imaginary part provides information of the propagation velocity of waves. Comparing (6) with the corresponding analytic counterpart

$$\frac{\mathrm{d}\widehat{U}}{\mathrm{d}t} = -\mathrm{i}ck\widehat{U}, \quad \mathrm{i} = \sqrt{-1}, \tag{7}$$

yields the phase speed of the numerical approximation

$$c^* = -\frac{\mathscr{I}m(H)}{k}. \tag{8}$$

It can be concluded that any dependency of c^* on the wave-number or propagation direction is erroneous. The ratio of numerical phase speed to true phase speed can be rewritten,

$$\frac{c^*}{c} = \frac{1}{kL}\left[s_\vartheta c_\varphi\sum_{j=0}^{N} a_{x,j}\sin(\vec{k}\cdot\vec{x}_j) + s_\vartheta s_\varphi\sum_{j=0}^{N} a_{y,j}\sin(\vec{k}\cdot\vec{x}_j) + c_\vartheta\sum_{j=0}^{N} a_{z,j}\sin(\vec{k}\cdot\vec{x}_j)\right], \tag{9}$$

where $\vec{k}$ stands for the wave-number vector $\vec{k} = k(s_\vartheta c_\varphi; s_\vartheta s_\varphi; c_\vartheta)^{\mathrm{T}}$, and $\vec{x}_j$ denotes the relative position of neighboring point j to point i. The abbreviations s_ϑ, c_ϑ, s_φ and c_φ have been used for the trigonometric functions $\sin\vartheta$, $\cos\vartheta$, $\sin\varphi$, and $\cos\varphi$, respectively. The group-velocity, defined as

$$v = \frac{\partial}{\partial k}(kc^*), \tag{10}$$

can be given in dimensionless form

$$\frac{v}{c} = \frac{1}{L}\left[s_\vartheta c_\varphi\sum_{j=0}^{N}(\vec{r}_0\cdot\vec{x}_j)a_{x,j}\cos(\vec{k}\cdot\vec{x}_j) + s_\vartheta s_\varphi\sum_{j=0}^{N}(\vec{r}_0\cdot\vec{x}_j)a_{y,j}\cos(\vec{k}\cdot\vec{x}_j) + c_\vartheta\sum_{j=0}^{N}(\vec{r}_0\cdot\vec{x}_j)a_{z,j}\cos(\vec{k}\cdot\vec{x}_j)\right], \tag{11}$$

with $\vec{r}_0 = (s_\vartheta c_\varphi; s_\vartheta s_\varphi; c_\vartheta)^{\mathrm{T}}$. For a spatial discretization to be non-dissipative, the real part of the spectral function has to vanish,

$$\mathscr{R}e(H) = -\frac{c}{L}\left[s_\vartheta c_\varphi \sum_{j=0}^{N} a_{x,j}\cos(\vec{k}\cdot\vec{x}_j) + s_\vartheta s_\varphi \sum_{j=0}^{N} a_{y,j}\cos(\vec{k}\cdot\vec{x}_j) + c_\vartheta \sum_{j=0}^{N} a_{z,j}\cos(\vec{k}\cdot\vec{x}_j)\right] = 0. \tag{12}$$

Restriction (12) must hold for any propagation angles ϑ and φ, which is only possible for a symmetric point arrangement, and antisymmetric coefficients a_x, a_y and a_z for a pair of symmetric points.

3. Requirements on differencing schemes for three-dimensional grid singularities

A three-dimensional grid singularity at an interior point P is characterized by the number of grid lines radiating from the point to be unequal to six. For the case of six lines, a Cartesian eight-block arrangement can be established and regular, one-dimensional differencing schemes can be used for each coordinate direction; if necessary, coordinate transformation accounts for non-orthogonal grid lines. If more or fewer branches radiate from point P, a regular differencing stencil cannot be used, and a geometrical singularity exists. It can be deduced that the number of blocks $\mathscr{M}$ joining in a particular point is linked to the number of branches $\mathscr{N}$ radiating from that point by

$$\mathscr{M} = 2(\mathscr{N} - 2), \quad \mathscr{N} \geqslant 4.$$

For example, five branches extending from P result in a six-block singularity. Consequently, an uneven number of joining blocks does not occur in three dimensions. In the current work, four-block (=four branches) and six-block (=five branches) singularities are treated. The eight-block arrangement refers to regular (Cartesian) differencing along the grid lines, hence, there is no need to treat it as a singularity. Higher grid singularities, as 10-block, and higher, are not followed in the present work. Table 1 gives an overview of the developed schemes.

Fig. 1 sketches the three-dimensional node arrangements of a four-block and a six-block singularity. A corner of a grid block is represented by three lines. Without loss of generality, the distance from P to its neighboring points is L. The tetrahedral arrangement of the four-block singularity exhibits an angle of $(\arccos(-\frac{1}{3}))$ between each pair of branches. The arrangement of the six-block singularity does not show the feature of same angles between each pair of branches. In fact, three points lay in the xy-plane, producing an angle of $(2\pi/3)$. The other two lines coincide with the z-axis.

As outlined in [1], differencing schemes for grid singularities are intended to be applied in those few points of a computational mesh, where regular differencing cannot be applied. Their spectral characteristics, as there are dispersive and dissipative properties, isotropy of phase speed, and the time-step limit, should fit to the characteristics of the schemes, which are used on the regular parts of the mesh. Consequently, the following issues have to be addressed:

- Non-dissipative approximation.
  There are two reasons to require this property: first, from physical point of view, wave propagation governed by the convection equation is non-dissipative, and it should also be reproduced by its discrete approximation. Second, any dissipation may cause numerical instability for a particular propagation direction, which is indicated in the complex plane by the spectralfunction of the scheme exceeding the stability region of the time-integration algorithm.

Table 1
Overview of the developed finite difference schemes for three-dimensional grid singularities. ("*point*" denotes number of positions involved in the differencing process)

Kind of singularity	Second order	Fourth order	Sixth order
4-block	14-point 8-point	28-point 16-point	42-point
6-block	20-point	46-point	–

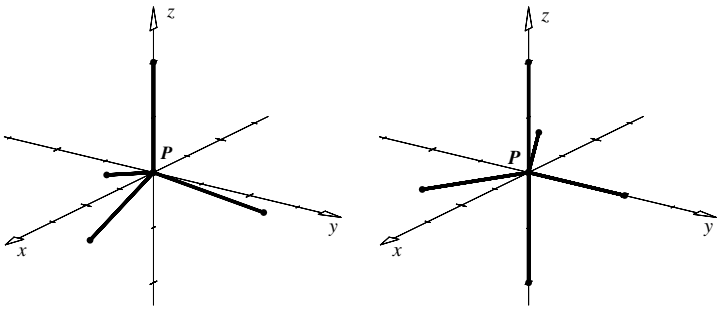

Fig. 1. Three-dimensional grid singularities. Left: four-block singularity; right: six-block singularity.

- Isotropy error of numerical phase velocity.
  The true phase speed is independent of propagation direction, which should also be mimicked by its approximation.
- Time-step limit.
  For explicit time integration, the time-step limit (in any direction) should be greater than the limit of the scheme used on the regular parts of the grid; i.e. the singular points, usually a few in number, should not limit the overall time-step of a computation.
- Formal order of accuracy. All the properties mentioned should be compatible with those of regular finite differences of the same order of accuracy, which are used on the structured parts of the computational mesh.

The coefficients multiplying the dependent variable at the discrete positions of the proposed schemes will be determined taking the described requirements into consideration. For the derivation of the coefficients it is assumed that the grid lines of each of the joining blocks are parallel in the vicinity of the singularity. Mesh distortion in practical problems can be taken into account by subsequent coordinate transformation.

For both treated singularities, the development of the difference scheme is discussed along the simplest case, i.e. the 14-point scheme for the four-block singularity, and the 8-point scheme for the six-block singularity, respectively (Table 1). Coefficients for higher order schemes will be given in Appendix.

4. Four-block singularities

4.1. Differencing stencil

As a consequence of the requirement for non-dissipative schemes, the real part of the spectral function (12) has to vanish. To accomplish this for any propagation direction, each point in the differencing stencil needs a symmetric point, which exhibits an antisymmetric coefficient. For example, the coefficients for a point at position $\vec{x}_1$ and its symmetric point at position $\vec{x}_2 = -\vec{x}_1$,

$$a_{x,1} = -a_{x,2},$$

to annihilate each other in the first sum of (12). For that reason, additional points have to be involved to build up a fully symmetric differencing stencil. Fig. 2 shows the arrangement with the introduced complementary points. The final stencil is made up by 14 points.

It has to be noted that points 6–8 and 12–14 are not located physically on the grid of one of the four joining blocks, i.e. the required positions are not located at grid line intersections. This fact will be taken into account by an appropriate coordinate transformation in Section 4.3, after the coefficients for the symmetric arrangement have been found in computational space. Table 2 gives the positions relative to point P in computational space (ξ, η, ζ).

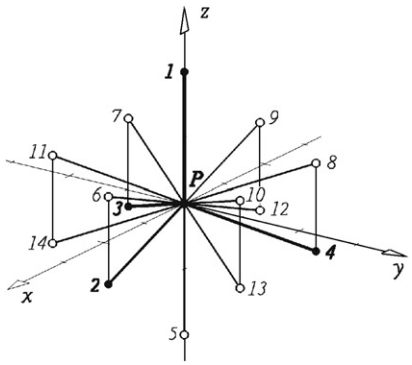

Fig. 2. Node arrangement for the four-block 14-point stencil. (Points symmetrical with respect to the *xy*-plane are connected to aid visibility.)

Table 2
Computational positions (ξ,η,ζ) of points for the four-block 14-point stencil

	1	2	3	4	5	6	7	8	9	10	11	12	13	14
ξ	0	$\frac{2\sqrt{2}}{3}$	$-\frac{\sqrt{2}}{3}$	$-\frac{\sqrt{2}}{3}$	0	$\frac{2\sqrt{2}}{3}$	$-\frac{\sqrt{2}}{3}$	$-\frac{\sqrt{2}}{3}$	$-\frac{2\sqrt{2}}{3}$	$\frac{\sqrt{2}}{3}$	$\frac{\sqrt{2}}{3}$	$-\frac{2\sqrt{2}}{3}$	$\frac{\sqrt{2}}{3}$	$\frac{\sqrt{2}}{3}$
η	0	0	$-\frac{\sqrt{6}}{3}$	$\frac{\sqrt{6}}{3}$	0	0	$-\frac{\sqrt{6}}{3}$	$\frac{\sqrt{6}}{3}$	0	$\frac{\sqrt{6}}{3}$	$-\frac{\sqrt{6}}{3}$	0	$\frac{\sqrt{6}}{3}$	$-\frac{\sqrt{6}}{3}$
ζ	1	$-\frac{1}{3}$	$-\frac{1}{3}$	$-\frac{1}{3}$	-1	$\frac{1}{3}$	$\frac{1}{3}$	$\frac{1}{3}$	$\frac{1}{3}$	$\frac{1}{3}$	$\frac{1}{3}$	$-\frac{1}{3}$	$-\frac{1}{3}$	$-\frac{1}{3}$

4.2. Derivation of coefficients for the 14-point scheme

Three-dimensional Taylor-series expansions of the dependent variable at the neighboring points around point P and subsequent term matching provides equations for determining the coefficients (=order conditions). The achievable order of accuracy is two in each coordinate direction. Furthermore, symmetry requirements for non-dissipative schemes give additional equations for the coefficients (=symmetry conditions). Taking all constraints (order conditions and symmetry conditions) into account, there remain one coefficient undetermined for the ξ-derivative, and two coefficients for the ζ-derivative. Those three open coefficients are too few to fulfill a further order of accuracy, and, consequently, will not be determined by term matching of Taylor-series expansions. Instead, the three undetermined coefficients are found by requiring the numerical phase velocity to be as isotropic as possible, i.e. the isotropy error of the numerical phase velocity is minimized. This optimization works on the expression for the numerical phase velocity as cost functional, with the undetermined coefficients as variables. They are chosen such that low order terms involving a dependency on propagation direction (ϑ,φ) are annihilated.

The following coefficients emerge:

$$\left.\frac{\partial U}{\partial \xi}\right|_P \approx \frac{1}{L}\sum_{j=1}^{14} a_{\xi,j}u_j, \quad \left.\frac{\partial U}{\partial \eta}\right|_P \approx \frac{1}{L}\sum_{j=1}^{14} a_{\eta,j}u_j, \quad \text{and} \quad \left.\frac{\partial U}{\partial \zeta}\right|_P \approx \frac{1}{L}\sum_{j=1}^{14} a_{\zeta,j}u_j, \tag{13}$$

with

$$\begin{aligned}
a_{\xi,j} &= \left\{0,\frac{\sqrt{2}}{8},\frac{-\sqrt{2}}{16},\frac{-\sqrt{2}}{16},0,\frac{\sqrt{2}}{8},\frac{-\sqrt{2}}{16},\frac{-\sqrt{2}}{16},\frac{-\sqrt{2}}{8},\frac{\sqrt{2}}{16},\frac{\sqrt{2}}{16},\frac{-\sqrt{2}}{8},\frac{\sqrt{2}}{16},\frac{\sqrt{2}}{16}\right\},\\
a_{\eta,j} &= \left\{0,0,\frac{-\sqrt{6}}{16},\frac{\sqrt{6}}{16},0,0,\frac{-\sqrt{6}}{16},\frac{\sqrt{6}}{16},0,\frac{\sqrt{6}}{16},\frac{-\sqrt{6}}{16},0,\frac{\sqrt{6}}{16},\frac{-\sqrt{6}}{16}\right\},\\
a_{\zeta,j} &= \left\{\frac{5}{16},\frac{-3}{32},\frac{-3}{32},\frac{-3}{32},\frac{-5}{16},\frac{3}{32},\frac{3}{32},\frac{3}{32},\frac{3}{32},\frac{3}{32},\frac{3}{32},\frac{-3}{32},\frac{-3}{32},\frac{-3}{32}\right\}.
\end{aligned} \tag{14}$$

The ratio of numerical phase speed to true phase speed (9) for the scheme in computational space is found to be

$$\frac{c^*}{c} = \frac{1}{8kL}\left\{ 3c_\vartheta \cos\left(\frac{2\sqrt{2}}{3} kLc_\varphi s_\vartheta\right) \sin\left(\frac{kL}{3} c_\vartheta\right) + 5c_\vartheta \sin(kLc_\vartheta) \right.$$
$$+ 4\sqrt{2} c_\varphi s_\vartheta \cos\left(\frac{kL}{3} c_\vartheta\right) \left[\cos\left(\sqrt{\frac{2}{3}} kLs_\varphi s_\vartheta\right) \sin\left(\frac{\sqrt{2}}{3} kLc_\varphi s_\vartheta\right) + \sin\left(\frac{2\sqrt{2}}{3} kLc_\varphi s_\vartheta\right) \right]$$
$$\left. + \cos\left(\frac{\sqrt{2}}{3} kLc_\varphi s_\vartheta\right) \left[6c_\vartheta \cos\left(\sqrt{\frac{2}{3}} kLs_\varphi s_\vartheta\right) \sin\left(\frac{kL}{3} c_\vartheta\right) + 4\sqrt{6} s_\varphi s_\vartheta \cos\left(\frac{kL}{3} c_\vartheta\right) \sin\left(\sqrt{\frac{2}{3}} kLs_\varphi s_\vartheta\right) \right] \right\}. \tag{15}$$

The leading term in the isotropy error of the numerical phase speed is

$$\epsilon = \frac{1}{72}\left(\frac{kL}{2}\right)^2 [29 + 3\cos(4\vartheta)] + \mathrm{HOT}, \tag{16}$$

with HOT denoting higher order terms. The error is independent of the circumferential angle φ up to second order, though it is dependent on ϑ. Fig. 3 shows the ratio of numerical to true phase speed for different dimensionless wavelengths λ/L for the scheme in computational space. Due to symmetry reasons, only the upper half of the distributions are plotted. The isotropy error for wavelengths $\lambda/L \geqslant 4$ is very small, i.e. the distribution of the phase velocity is similar to a half-sphere.

4.3. Transformation to physical grid

The proposed finite difference scheme has been developed for a differencing stencil, whose points do not all coincide with grid line intersections of the four adjacent blocks; namely, the points 6–8 and 12–14 lie

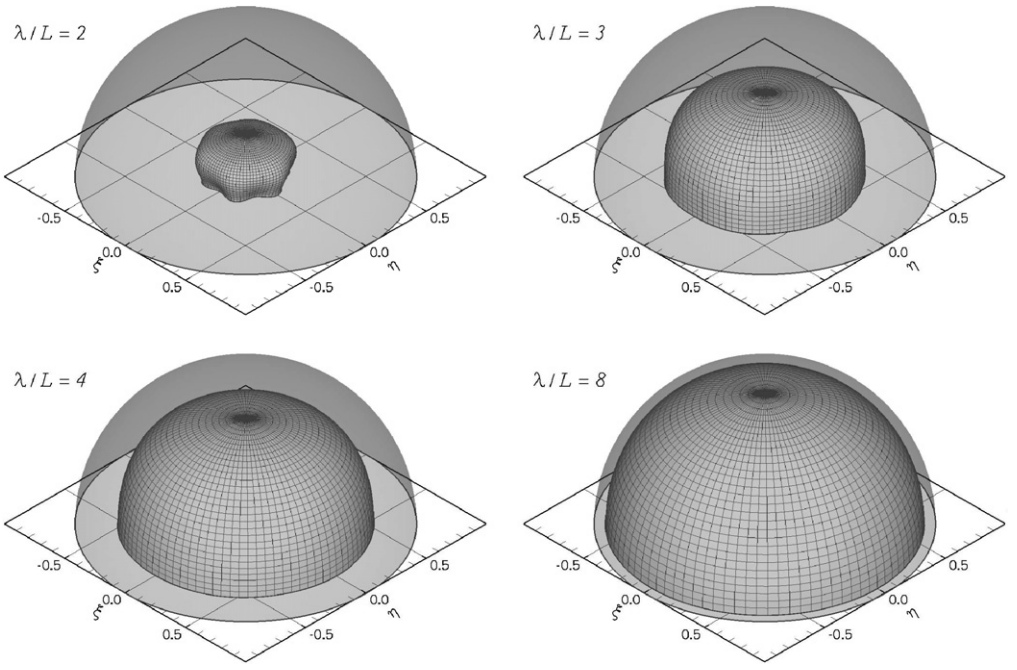

Fig. 3. Normalized numerical phase velocity c^*/c for several dimensionless wavelengths λ/L for the four-block 14-point scheme in computational space. (Transparent surface denotes the exact value of unity.)

in-between grid lines. Coordinate transformation is used to map the points of the differencing stencil in computational space to the physical grid. For example,

$$\frac{\partial U}{\partial x} = \xi_x \frac{\partial U}{\partial \xi} + \eta_x \frac{\partial U}{\partial \eta} + \zeta_x \frac{\partial U}{\partial \zeta}, \tag{17}$$

where ξ, η and ζ are the coordinates in computational space, and subscripts denote derivation with respect to the corresponding Cartesian direction. Metrics is found by the transformation Jacobi-matrix using the proposed differencing scheme. The Jacobi-matrix is found to be

$$J = \frac{\partial(\xi,\eta,\zeta)}{\partial(x,y,z)} = \begin{pmatrix} 1 & 0 & 0 \\ 0 & 1 & 0 \\ 0 & 0 & \frac{16}{19} \end{pmatrix}. \tag{18}$$

Due to the diagonal form of the Jacobi-matrix, the derivatives in physical space reduce to

$$\begin{aligned} \frac{\partial U}{\partial x} &= \frac{\partial U}{\partial \xi} \approx \frac{1}{L}\sum_{j=1}^{14} a_{\xi,j} u_j, \\ \frac{\partial U}{\partial y} &= \frac{\partial U}{\partial \eta} \approx \frac{1}{L}\sum_{j=1}^{14} a_{\eta,j} u_j, \\ \text{and} \quad \frac{\partial U}{\partial z} &= \zeta_z \frac{\partial U}{\partial \zeta} \approx \frac{16}{19}\left(\frac{1}{L}\sum_{j=1}^{14} a_{\zeta,j} u_j\right). \end{aligned} \tag{19}$$

The proposed method of developing the coefficients avoids any interpolation of the dependent variable at positions between grid line intersections. Apparently, the coordinate transformation does not change the non-dissipative nature of the scheme. Hence, the scheme will be numerically stable for all directions of propagation, provided, the CFL-limit is met.

4.4. 28-point scheme and 42-point scheme

Higher order schemes can be constructed by involving additional points in the differencing stencil, considering that the node arrangement has to be symmetric with respect to the coordinate axes. This can be achieved by, e.g. placing an additional point in a distance of $2L$ from the central point P along each branch, resulting in a 28-point scheme. In a very similar way, a 42-point scheme can be constructed by extending each branch by a further point. The numbering system follows the systematic of the 14-point stencil, so that point 15 lies on the extended branch through 1, point 16 corresponds to 2, and so on.

The equations for determining the coefficients a_ξ, a_η and a_ζ are established in the same way as for the 14-point scheme by Taylor-series expansion and symmetry conditions for non-dissipative schemes. The achievable formal order of accuracy is four for the 28-point scheme, and six for the 42-point scheme, respectively. Again, there are not yet sufficient equations to determine all coefficients: for both the 28-point and 42-point scheme, one coefficient of the a_ξ-set and two coefficients of the a_ζ-set remain undetermined. Additional equations are provided by minimizing the dependency of the numerical phase speed from propagation direction. The coefficients for both schemes are given in Appendices A.1 and A.2, respectively.

Due to reasons of space, explicit expression for the ratios of numerical phase speed to true phase speed are not given here; the leading terms of the phase speed errors are given in Appendix, as well as the transformation Jacobi-matrix for both schemes. Results for the 28-point scheme for different dimensionless wavelengths are presented in Fig. 4.

Owing to the minimization of the isotropy error, the numerical phase speed is already very isotropic for wavelengths $\lambda/L \geqslant 3$.

The absolute value of the numerical phase velocity in transformed physical space for a dimensionless wavelength ($\lambda/L = 8$) is

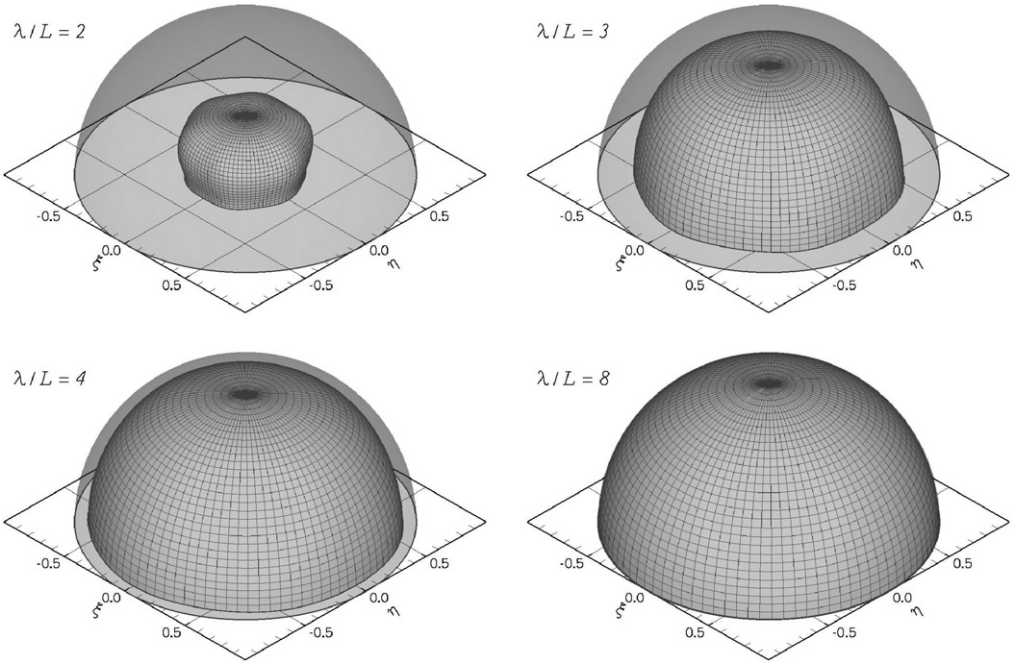

Fig. 4. Normalized numerical phase velocity c^*/c for several dimensionless wavelengths λ/L for the four-block 28-point scheme in computational space. (Transparent surface denotes the exact value of unity.)

$$0.989983 \leqslant c^* \leqslant 0.994636, \tag{20}$$

which is a very good approximation compared to the exact value of one. The corresponding value for a regular finite difference of the same order of accuracy, for instance the 12-point central difference, is

$$0.988215 \leqslant c^* \leqslant 0.998624. \tag{21}$$

This indicates that the proposed approximation for a first derivative for the grid singularity is compatible in terms of phase speed with a differencing scheme, which may be used on the regular part of the computational grid.

For the 42-point scheme plots of the ratio of numerical phase speed to true phase speed for different wavelengths are shown in Fig. 5. Apparently, the absolute value of the phase speed as well as its isotropy error are improved compared to the 28-point scheme.

For a wavelength ($\lambda/L = 8$), the value of the numerical phase speed on the physical grid, i.e. after the transformation of the developed scheme from computational to physical space, is

$$0.998401 \leqslant c^* \leqslant 0.999541, \tag{22}$$

which compares very well with the value of the corresponding central difference approximation of sixth order,

$$0.998513 \leqslant c^* \leqslant 0.999940. \tag{23}$$

Table 3 presents an overview of the resolution capabilities in terms of phase velocity for the four-block schemes. The minimum wavelengths are given, which exhibit a certain error in phase speed ϵ_c,

$$\epsilon_c = 1 - \frac{c^*}{c},$$

in comparison with three-dimensional Cartesian schemes of the same order of accuracy. Obviously, the resolution capabilities are very similar to standard approximations.

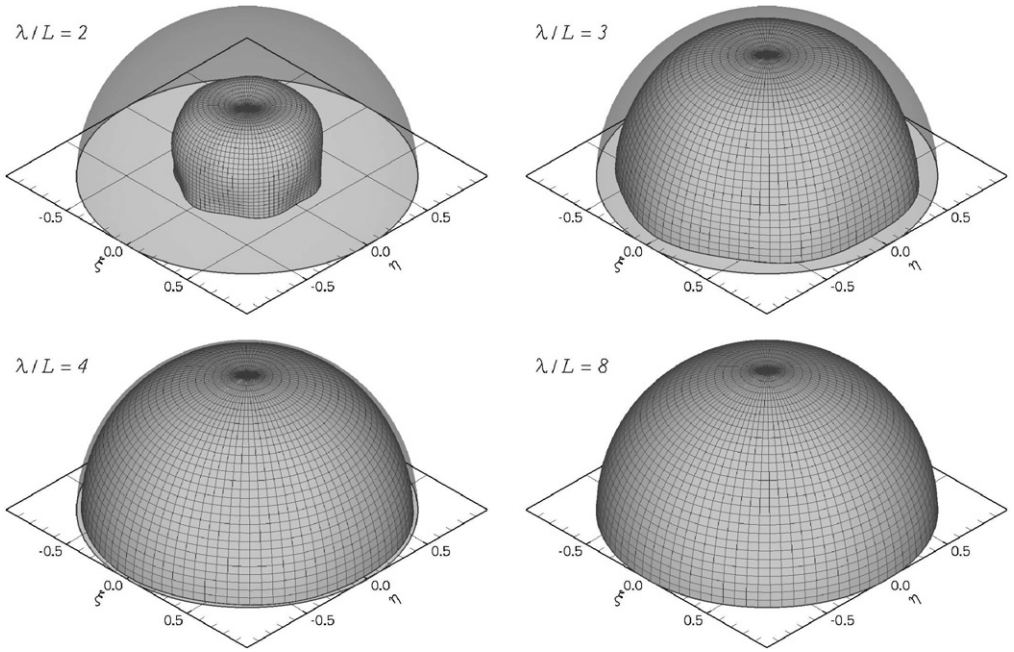

Fig. 5. Normalized numerical phase velocity c^*/c for several dimensionless wavelengths λ/L for the four-block 42-point scheme in computational space.

Table 3
Resolution capabilities on physical grid of schemes for the four-block singularity and corresponding central finite differences involving 6, 12, and 18 points, respectively (=cds-6, -12, and -18) for different errors in phase speed ϵ_c

	Order	$\epsilon_c = 0.01$	$\epsilon_c = 0.001$
14-point	2	$\lambda/L \geqslant 22.49$	$\lambda/L \geqslant 71.25$
28-point	4	8.01	14.47
42-point	6	5.75	8.69
cds-6	2	25.61	81.10
cds-12	4	8.35	15.19
cds-18	6	5.71	8.57

5. Six-block singularities

For the six-block singularity two second order schemes (8-point and 20-point) and two fourth order schemes (16-point and 46-point) have been developed.

5.1. Second order schemes

As for the differencing stencils for four-block singularities, additional points are introduced to generate symmetric differencing molecules for six-block singularities. In the simplest case, only diagonal points in the xy-plane have to be introduced to create an 8-point stencil, Fig. 6.

Since all points lie on grid line intersections, no subsequent coordinate transformation will be necessary. The differencing molecule is very similar to the stencil for a two-dimensional three-way singularity proposed in [1] and in [12]; it has just been extended in the third direction by a two-point central difference. The attainable formal order of accuracy is two in all coordinate directions. One coefficient for the derivative in y-direction remains undetermined, it is found in the described way of minimizing the directional dependency of the numerical phase speed. The resulting coefficients are

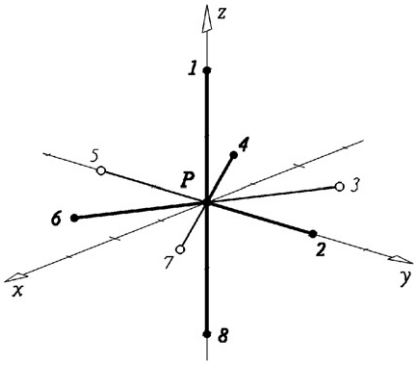

Fig. 6. Node arrangement for the six-block 8-point stencil.

$$a_{x,i} = \left\{0, 0, \frac{-\sqrt{3}}{6}, \frac{-\sqrt{3}}{6}, 0, \frac{\sqrt{3}}{6}, \frac{\sqrt{3}}{6}, 0\right\}, \quad a_{y,i} = \left\{0, \frac{1}{3}, \frac{1}{6}, -\frac{1}{6}, -\frac{1}{3}, -\frac{1}{6}, \frac{1}{6}, 0\right\},$$
$$\text{and} \quad a_{z,i} = \left\{\frac{1}{2}, 0, 0, 0, 0, 0, 0, -\frac{1}{2}\right\}. \tag{24}$$

The leading term of the isotropy error is independent of the circumferential angle φ,

$$\epsilon = \frac{1}{48}\left(\frac{kL}{2}\right)^2 \{4\cos(2\vartheta) + 7[3 + \cos(4\vartheta)]\} + \text{HOT}. \tag{25}$$

The ratio of numerical phase speed to true phase speed is

$$\frac{c^*}{c} = \frac{1}{3kL}\left\{3c_\vartheta \sin(c_\vartheta kL) + 2s_\vartheta\left[\sqrt{3}c_\varphi \cos\left(\frac{kL}{2}s_\varphi s_\vartheta\right)\sin\left(\frac{\sqrt{3}}{2}kLc_\varphi s_\vartheta\right)\right.\right.$$
$$\left.\left. + s_\varphi \sin\left(\frac{kL}{2}s_\varphi s_\vartheta\right)\cos\left(\frac{\sqrt{3}}{2}kLc_\varphi s_\vartheta\right) + s_\varphi \sin(kLs_\varphi s_\vartheta)\right]\right\}, \tag{26}$$

Fig. 7 illustrates the result. In view of the fact that only eight points are involved in the differencing process, the result is quite good regarding isotropy.

Involving additional points, a symmetric 20-point scheme can be constructed, Fig. 8. All points are located at grid line intersections, making a subsequent coordinate transformation unnecessary. Taking order and symmetry constraints into account, there remain six coefficients undetermined for the 20-point scheme (one for the x-direction, three for the y-direction and two for the z-direction, respectively). Again, the undetermined coefficients are found by minimizing the directional dependency of the numerical phase velocity. The resulting set of coefficients is listed in Appendix B.1, where the leading error term of the numerical phase velocity is also given. Fig. 9 shows the ratio of numerical phase speed to true phase speed for the 20-point scheme. The numerical phase speed is clearly improved in terms of isotropy, but its absolute value is even smaller than for the comparable 8-point scheme. Obviously, only the involvement of points farther distant from P yield a reduction of the absolute phase speed error.

5.2. Higher order schemes

Fourth order schemes have been constructed by involving additional points in the differencing molecule. In the simplest case, the 8-point scheme is extended by one further point along each branch producing a symmetric 16-point scheme, which is fourth order accurate. Basically, the resulting scheme is a two-dimensional finite difference proposed in [1], which has been extended by a fourth order central difference in z-direction. Appendix B.2 provides the coefficients and the leading error term; plots of the numerical phase speed are shown in

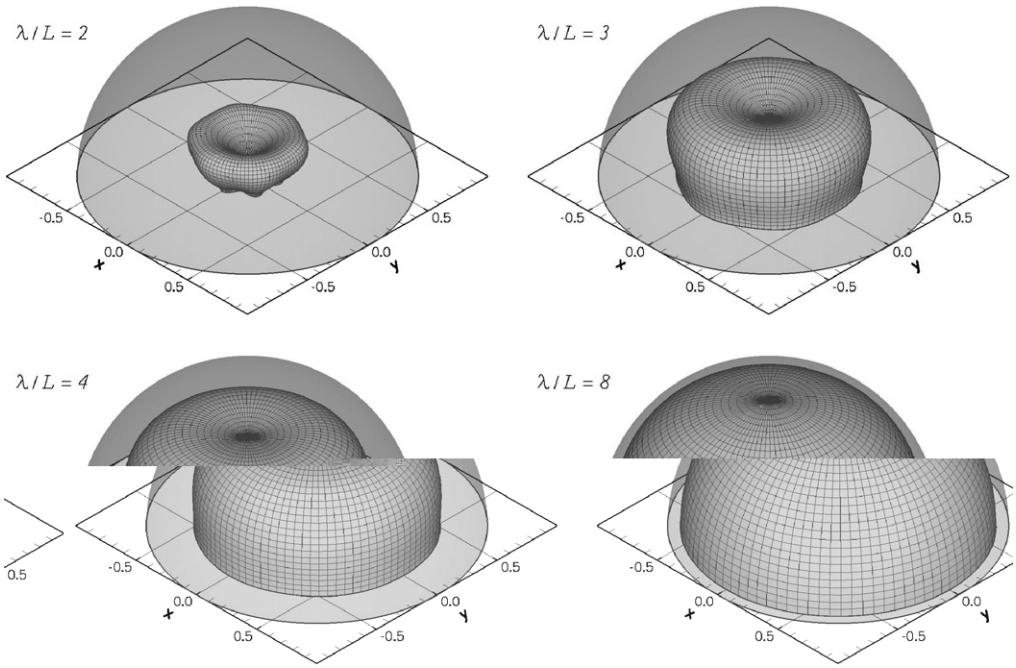

Fig. 7. Normalized numerical phase velocity c^*/c for several dimensionless wavelengths λ/L for the six-block 8-point scheme.

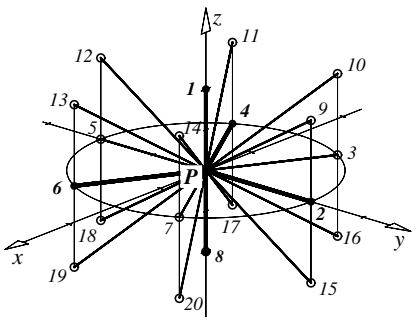

Fig. 8. Node arrangement for the six-block 20-point stencil. (Points located in the xy-plane and points symmetrical with respect to the xy-plane are connected to aid visibility.)

Fig. 10. The absolute value of the phase speed is considerably improved. It is interesting to note that better results are achieved by involving four points less than in the 20-point scheme, despite the fact that the current scheme is of fourth order accuracy and the latter is second order.

Several attempts have been made to increase the accuracy by extending each branch of the 20-point scheme by an additional point, producing a 40-point stencil. It has to be reported that no significant improvement compared to the 16-point scheme has been found. On the contrary, the optimization process yield the coefficients for the 16-point scheme, setting the other coefficients to zero. This implies that the 16-point scheme is a very good compromise between the number of points involved and the achievable accuracy.

Improvement is found by adding six more points to the 40-point arrangement, giving a 46-point stencil. The added points are located in the xy-plane diagonally between the points 2 and 3, 3 and 4, and so on. The formal order of accuracy stays with four, the nine undetermined coefficients (two of the a_x-set, five of the a_y-set, and two of the a_z-set, respectively) are found in the described way, the coefficients are listed in Appendix B.3. It is interesting to note that the optimization process yields many coefficients to be zero, i.e. those points are obsolete in the differencing process. In fact, the 46-point scheme reduces to a scheme with 22 points of non-zero

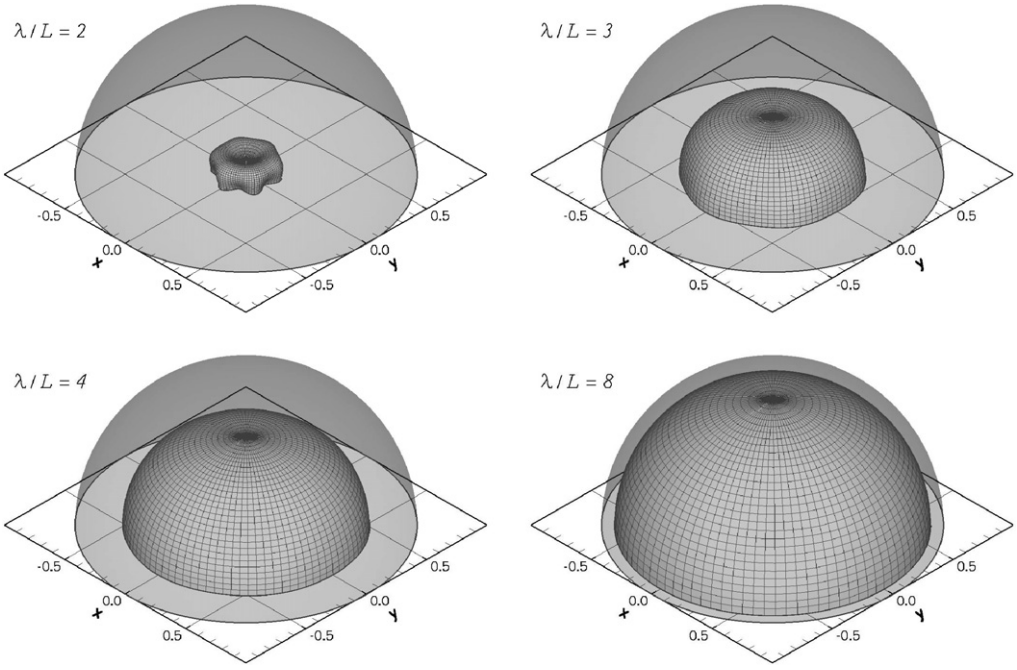

Fig. 9. Normalized numerical phase velocity c^*/c for several dimensionless wavelengths λ/L for the 20-point scheme.

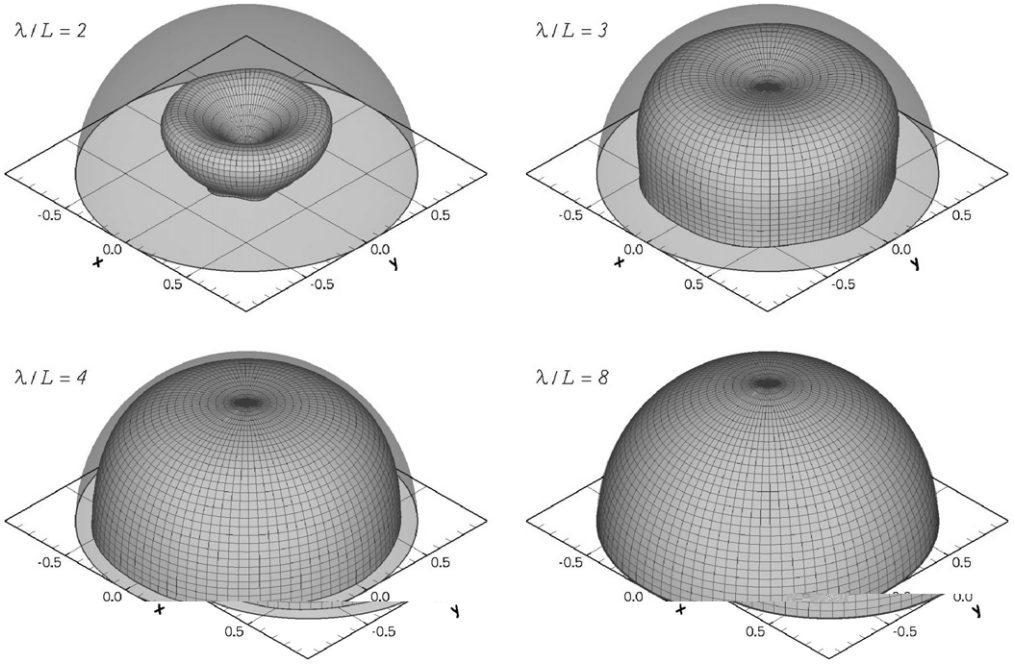

Fig. 10. Normalized numerical phase velocity c^*/c for several dimensionless wavelengths λ/L for the six-block 16-point scheme.

coefficients. Fig. 11 plots the distribution of the ratio of numerical to true phase speed for the usual dimensionless wavelengths. The absolute value of the numerical phase speed has increased compared to the 16-point scheme.

For a dimensionless wavelength of $\lambda/L = 8$, the value of the numerical phase speed is

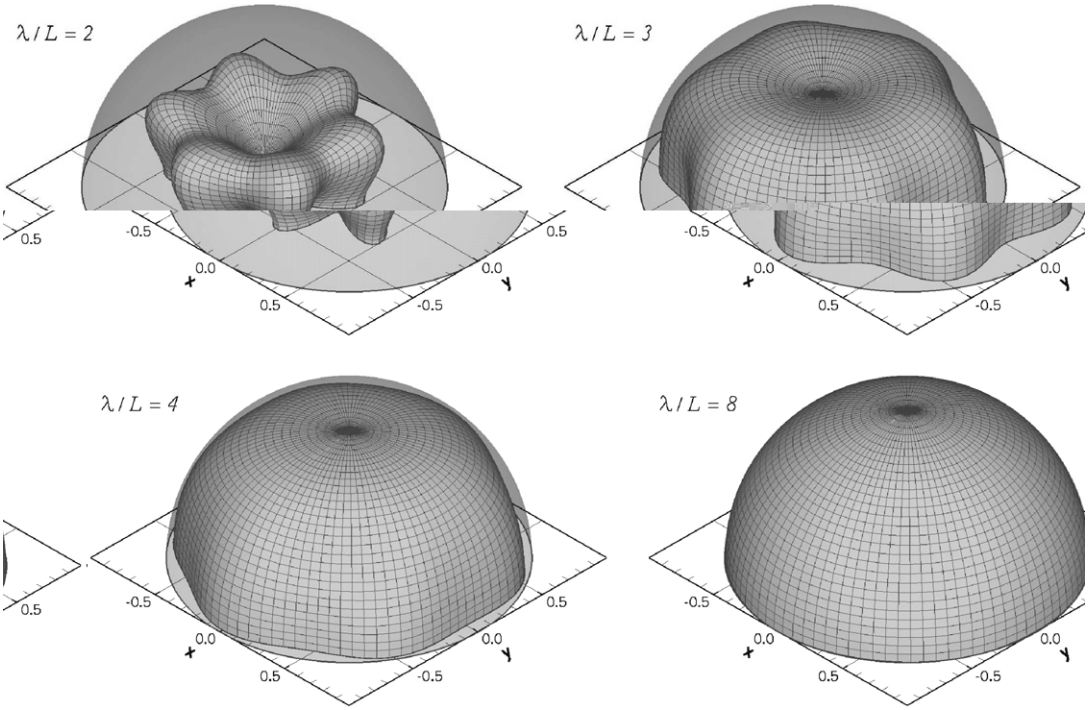

Fig. 11. Normalized numerical phase velocity c^*/c for several dimensionless wavelengths λ/L for the six-block 46-point scheme.

$$0.988215 \leqslant c^* \leqslant 0.999391, \tag{27}$$

being slightly greater than the value of the central differencing scheme of order four,

$$0.988215 \leqslant c^* \leqslant 0.998624. \tag{28}$$

The resolution capabilities in terms of phase speed of the schemes for the six-block singularity are compared to central differences in Table 4. The schemes for grid singularities show the same resolution limits as corresponding central differences. It can be concluded that the central difference in z-direction is responsible for that fact, and that the rest of the approximation achieves higher accuracy.

6. Stability limits

Stability limits for explicit time integration have been investigated based on the three-dimensional linear convection Eq. (1) and the classical four-stage Runge–Kutta scheme of fourth order to advance in time. Conversion of the time-step limits to any other explicit time-integration scheme is straightforward. Spatial Fourier transformation of the semi-discretized equation provides information about numerical stability of the algorithm. The autonomous system (6)

Table 4
Resolution capabilities of schemes for a six-way singularity and corresponding central finite differences involving 6 and 12 points (= cds-6 and -12) for different errors in phase speed ϵ_c

	Order	$\epsilon_c = 0.01$	$\epsilon_c = 0.001$
8-point	2	$\lambda/L \geqslant 25.61$	$\lambda/L \geqslant 81.10$
20-point	2	25.61	81.10
16-point	4	8.35	15.02
46-point	4	8.35	15.02
cds-6	2	25.61	81.10
cds-12	4	8.35	15.02

$$\frac{\mathrm{d}\hat{u}}{\mathrm{d}t} = H(k,\vartheta,\varphi)\hat{u}$$

is integrated by the aforementioned scheme; the resulting amplification factor is

$$G(k,\vartheta,\varphi,\Delta t) = \frac{\hat{u}^{n+1}}{\hat{u}^n} = 1 + \sum_{j=1}^{4} \frac{(\Delta t H)^j}{j!}. \tag{29}$$

Stability in the von Neumann sense (e.g. [13]) is found, if

$$|G(k,\vartheta,\varphi,\Delta t)| \leqslant 1. \tag{30}$$

From the stability condition (30) the time-step limit for the particular spectralfunction $H(k,\vartheta,\varphi)$ can be evaluated for a given propagation direction (ϑ,φ) and dimensionless wave-number k.

As discussed in Section 3, the time-step limits of the proposed schemes should be greater than the limits of the schemes on the regular mesh. The usually small number of singular points should not dictate the overall time-step limit of a computation. For that reason, the smallest time-step limit in any direction has been evaluated for each scheme. Table 5 compares the time-step limits to those of central differences of the same order of accuracy.

Evidently, all schemes – except the six-block 46-point scheme – exhibit greater time-step limits than the corresponding central differences. The 46-point scheme has a slightly smaller time-step limit, which probably does not play a significant role in practical applications.

It has to be noted that the time-step limits for both the schemes for singular and regular grid points have been evaluated using the same point-to-point distance. Mesh distortion changes the actual time-step limit in general.

7. Numerical experiments

7.1. Verification of the formal order of accuracy

The formal order of accuracy is evaluated using the three-dimensional linear convection equation (1). The computational domain consists of a cube with a side-length of 40; in each coordinate direction 41 equally distributed points are modeled resulting in a point-to-point distance of one along the grid lines. The initial Gaussian distribution

$$U(\vec{x},0) = \exp\left[-\ln 2\frac{|\vec{x}-\vec{x_c}|^2}{3^2}\right], \quad \text{with } \vec{x_c} = (20;20;20)^{\mathrm{T}},$$

is transported in diagonal direction with a propagation velocity $|\vec{c}| = 1$. Periodic boundaries are applied at the borders of the domain to avoid any influence of boundary formulations and discretizations on the numerical behavior of the scheme under investigation. It has to be noted that neither of the proposed schemes applies directly to a Cartesian grid, i.e. the point locations of the stencils do not coincide with grid line intersections of the Cartesian mesh. Therefore, the stencils are distorted to match the Cartesian positions, and a coordinate

Table 5
Time-step limits of central differences and schemes for singular points based on explicit Runge–Kutta integration of fourth order

	Regular	Singular, 4-block	Singular, 6-block	
Second order	cds-6	14-point	8-point	20-point
	1.6330	2.1767	1.8347	2.4104
Fourth order	cds-12	28-point	16-point	46-point
	1.1900	1.6538	1.3495	1.1422
Sixth order	cds-18	42-point	–	–
	1.0300	1.4558	–	–

cds-6 denotes central difference involving six points, etc.

transformation is employed to account for that. This coordinate transformation uses the same differencing scheme which is currently investigated. In that way the error reduction can be evaluated, though the absolute level of the error can hardly be compared, since each coordinate transformation introduces a different error according to the particular distortion of the stencil.

Time is integrated explicitly by the classical four-stage Runge–Kutta scheme of fourth order, keeping the Courant-number constant at 0.1 for all calculations. If the Courant-number was chosen too great, the decrease of the error would reflect the order of time-integration rather than the spatial discretization in the case of the sixth order scheme. Preliminary numerical experiments proved such a Courant-number to be sufficiently small for the error of time-integration not to corrupt the spatial error. At time $t = 35$ the numerical solution is compared with the analytical one. Subsequent grid refinement with a factor of two is applied to evaluate the reduction of the global error, which is measured by the L_2-norm of the local errors,

$$L_2 = \sqrt{\sum_i (u_i - U_i)^2},$$

where U_i denotes the analytical solution at the discrete position i at time $t = 35$. The error reduction of both the schemes for four-block and six-block singularities are presented in Fig. 12. With subsequent grid refinement, the errors of the schemes reduce with the proposed order.

7.2. Acoustic source above a plane wall

As an example for the application of the proposed schemes the scattering of sound from an acoustic source above a plane wall is examined. The propagation of sound is described by the linearized Euler equations in dimensionless form,

$$\begin{aligned} &\frac{\partial \rho}{\partial t} + \nabla \cdot \vec{v} = 0, \\ &\frac{\partial \vec{v}}{\partial t} + \nabla p = 0, \\ &\frac{\partial p}{\partial t} + \nabla \cdot \vec{v} = S, \end{aligned} \tag{31}$$

with the harmonic source

$$S = \exp\left[-\ln 2 \frac{|\vec{x} - \vec{x_c}|^2}{r^2}\right] \sin(\omega t),$$

where density ρ, pressure p and velocity $\vec{v}$ have been non-dimensionalized by ambient density, pressure and speed of sound. For the source a time frequency of $\omega = 2\pi/3$ and a half-height radius $r = 2$ is chosen. The center of the source is located in $\vec{x}_c = (20; 20; 20)^{\mathrm{T}}$. The geometry consists of a cube with a side-length of

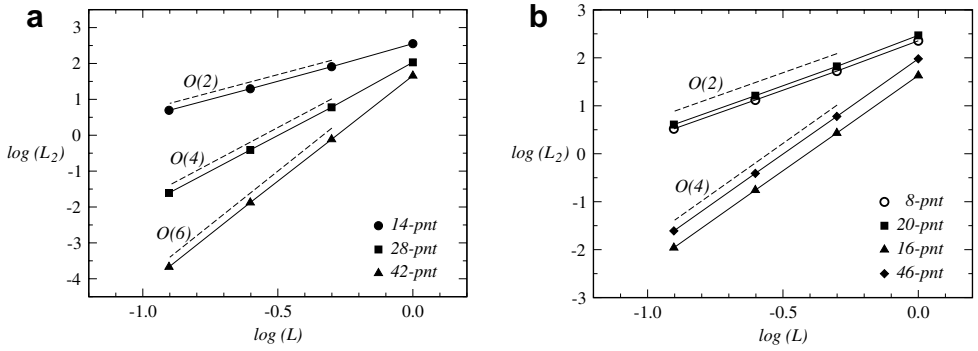

Fig. 12. Reduction of global error with grid refinement: (a) schemes for four-block singularities, (b) schemes for six-block singularities. (Dashed lines denote slopes of 2, 4, and 6 in logarithmic scale.)

40 and 161 equally spaced points along each coordinate direction. At the bottom boundary, a wall is prescribed; the other boundaries exhibit radiation condition for the acoustic waves.

To examine the performance of the proposed schemes, they are used together with central differences of the same order of accuracy; 40 randomly distributed points are treated with the singular schemes where the rest of the grid is computed using regular schemes of the same order. Fig. 13 shows a plot of the acoustic pressure at time $t = 70$. The numerically obtained results are compared with the analytic solution along the line $x = z = 20$ for $t = 70$; Fig. 14 shows the results. The analytic solution is found using free-space Green's function for the wave-equation; a mirror source is applied to account for the wall. Despite the fact that the peak of the signal is reproduced slightly to small, all numerical solutions compare quite well with the analytical one. Magnification reveals the behavior of the numerical solutions, Fig. 15. Apparently, the calculation grid is not fine enough to use second order schemes; The amplitudes in the numerical solutions are to small. Nevertheless, the calculations with the singular schemes are very similar to that using only regular schemes. The fourth order schemes approximate the analytical solution well; only small deficiencies in amplitude are found. It is interesting to note that all schemes used – regular and singular – are non-dissipative. Hence, the reduction in amplitude originates from discretizations at the boundary, where biased schemes have to be used, and from time integration. The sixth order calculations reproduce the exact solution very well. The drifting of the pressure near the boundary is due to the lower order, one-sided schemes used for boundary points. The numerical solutions with the singular schemes present shows no discernible differences to the calculation using only regular schemes.

8. Discussion of the proposed schemes

The proposed schemes have been developed for grid singularities, which represent a small number of points in a computational grid compared to the number of points for which regular differencing can be applied. For

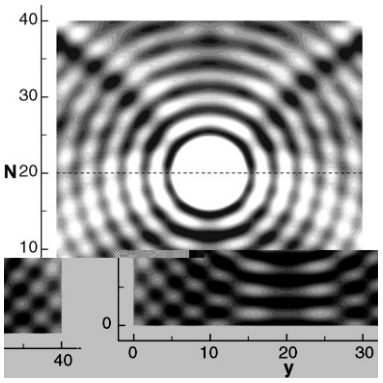

Fig. 13. Acoustic pressure at $t = 70$ and $x = 20$. (Dashed line denotes position for comparison with analytic solution.)

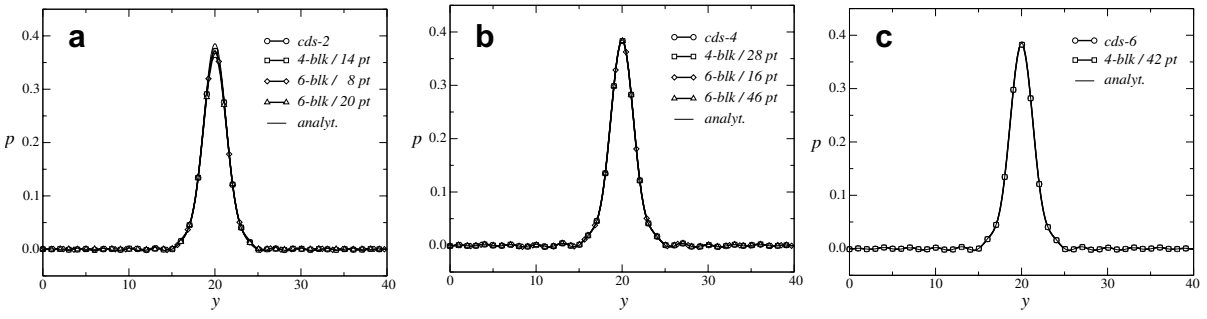

Fig. 14. Comparison of numerical solutions with the analytical one at $x = z = 20$, and for $t = 70$: (a) second-, (b) fourth-, and (c) sixth-order schemes. (cds-2 denotes numerical calculation using only second order central differences, etc.)

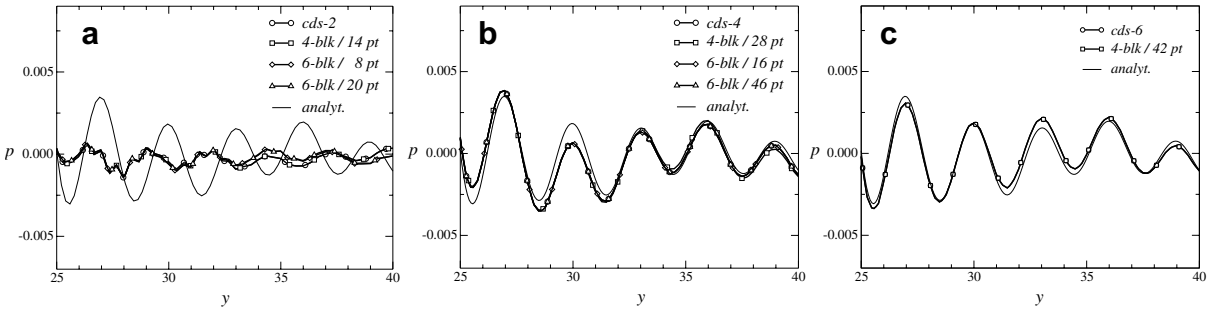

Fig. 15. Detail of pressure distribution. (a) second-, (b) fourth-, and (c) sixth-order schemes.

that reason, their spectral characteristics should fit to those of regular schemes. For explicit time integration, the time-step limit is also an issue; it should not limit the overall time-step of the computation. The proposed schemes fulfill all those requirements when compared to central differencing schemes of the same order of accuracy. This may not necessarily be the case for other types of high order schemes, as compact schemes.

The administrative and computational effort of the proposed higher order schemes, especially with more than 20 points, seems to be high, but there is usually a very limited number of points, which have to be treated in that way. Nevertheless, it has been shown, that for the six-block singularity the improvement of the 46-point scheme in absolute phase speed is very small compared to the much simpler 16-point scheme; despite the fact that the latter has a higher time-step limit. The increase of computational costs is proportional to the number of points treated by singular schemes. Compared to Cartesian schemes, a factor of 7/3 (four-block schemes) and 4/3 to 10/3 (six-block schemes) can be deduced.

Two remarks concerning the optimization process are in order. First, the open coefficients of the schemes are found by minimizing the isotropy error of the phase velocity. For that process, more than one minimum can exist and have been found. The coefficients represent one minimum, which was chosen by taking the time-step limit into account as well; it would be contradictory to choose the coefficients merely according to excellent phase speed isotropy and get a very small stability limit on the other hand.

Second, for the schemes for four-block singularities, optimization has been performed in computational space. Coordinate transformation maps the schemes to physical space, whereas this transformation employs the developed scheme. Consequently, the schemes are not optimized in physical but in computational space. Nevertheless, the spectral characteristics of the final schemes are very satisfactory. A comparison of the resolution capabilities shows that the proposed schemes are able to resolve waves as accurate as regular schemes do. This indicates that they can be well combined with regular schemes of the same order of accuracy.

9. Summary and conclusion

Explicit finite difference approximations for first derivatives with three-dimensional non-regular stencils have been developed. They are intended to be used in singular points of three-dimensional computational grids, where regular differencing is not possible. Open coefficients, which are too few in number to fulfill a further order of accuracy, are determined by optimizing the isotropy error of the numerical phase speed. Due to their symmetric node arrangement the coefficients could be chosen to result in non-dissipative schemes.

For a four-block singularity, a second, fourth and sixth order scheme have been developed in computational space, and mapped to the physical grid arrangement by coordinate transformation. For six-block, two second order and two fourth order schemes are proposed.

Owing to the objective of the optimization process, both the numerical phase speeds and the time-step limits exhibit high isotropy. Further, all schemes (except one) exhibit applicable time steps which are greater than those of comparable central differences.

Conclusively, the proposed finite difference schemes could improve a major drawback of finite difference schemes, namely their inflexibility of treating computational meshes with grid singularities.

Appendix A. Four-block singularities

A.1. Fourth-order 28-point scheme

The coefficients are found to be

$$a_{\xi,j} = \left\{0, \frac{\sqrt{2}}{6}, \frac{-\sqrt{2}}{12}, \frac{-\sqrt{2}}{12}, 0, \frac{\sqrt{2}}{6}, \frac{-\sqrt{2}}{12}, \frac{-\sqrt{2}}{12}, \frac{-\sqrt{2}}{6}, \frac{\sqrt{2}}{12}, \frac{\sqrt{2}}{12}, \frac{-\sqrt{2}}{6}, \frac{\sqrt{2}}{12}, \frac{\sqrt{2}}{12}, \right.$$
$$\left. 0, \frac{-\sqrt{2}}{48}, \frac{\sqrt{2}}{96}, \frac{\sqrt{2}}{96}, 0, \frac{-\sqrt{2}}{48}, \frac{\sqrt{2}}{96}, \frac{\sqrt{2}}{96}, \frac{\sqrt{2}}{48}, \frac{-\sqrt{2}}{96}, \frac{-\sqrt{2}}{96}, \frac{\sqrt{2}}{48}, \frac{-\sqrt{2}}{96}, \frac{-\sqrt{2}}{96}\right\},$$

$$a_{\eta,j} = \left\{0, 0, \frac{-\sqrt{6}}{12}, \frac{\sqrt{6}}{12}, 0, 0, \frac{-\sqrt{6}}{12}, \frac{\sqrt{6}}{12}, 0, \frac{\sqrt{6}}{12}, \frac{-\sqrt{6}}{12}, 0, \frac{\sqrt{6}}{12}, \frac{-\sqrt{6}}{12}, 0, 0, \frac{\sqrt{6}}{96}, \frac{-\sqrt{6}}{96}, \right.$$
$$\left. 0, 0, \frac{\sqrt{6}}{96}, \frac{-\sqrt{6}}{96}, 0, \frac{-\sqrt{6}}{96}, \frac{\sqrt{6}}{96}, 0, \frac{-\sqrt{6}}{96}, \frac{\sqrt{6}}{96}\right\},$$

$$a_{\zeta,j} = \left\{\frac{3}{8}, \frac{-7}{48}, \frac{-7}{48}, \frac{-7}{48}, \frac{-3}{8}, \frac{7}{48}, \frac{7}{48}, \frac{7}{48}, \frac{7}{48}, \frac{7}{48}, \frac{7}{48}, \frac{-7}{48}, \frac{-7}{48}, \frac{-7}{48}, \right.$$
$$\left. \frac{-3}{64}, \frac{7}{384}, \frac{7}{384}, \frac{7}{384}, \frac{3}{64}, \frac{-7}{384}, \frac{-7}{384}, \frac{-7}{384}, \frac{-7}{384}, \frac{-7}{384}, \frac{-7}{384}, \frac{7}{384}, \frac{7}{384}, \frac{7}{384}\right\}.$$

The leading term in the isotropy error of the numerical phase speed is of fourth order,

$$\epsilon = \frac{1}{2430}\left(\frac{kL}{2}\right)^4 [565 + 123\cos(4\vartheta) + 48\cos(6\vartheta) + 64\cos(6\varphi)\sin^6\vartheta] + \text{HOT}. \tag{A.1}$$

The Jacobi-matrix to transform the differencing scheme to the physical grid is found to be

$$J = \begin{pmatrix} 1 & 0 & 0 \\ 0 & 1 & 0 \\ 0 & 0 & \frac{32}{39} \end{pmatrix}. \tag{A.2}$$

A.2. Sixth-order 42-point scheme

The coefficients are found to be

$$a_{\xi,j} = \left\{0, \frac{3\sqrt{2}}{16}, \frac{-3\sqrt{2}}{32}, \frac{-3\sqrt{2}}{32}, 0, \frac{3\sqrt{2}}{16}, \frac{-3\sqrt{2}}{32}, \frac{-3\sqrt{2}}{32}, \frac{-3\sqrt{2}}{16}, \frac{3\sqrt{2}}{32}, \frac{3\sqrt{2}}{32}, \frac{-3\sqrt{2}}{16}, \frac{3\sqrt{2}}{32}, \frac{3\sqrt{2}}{32}, \right.$$
$$0, \frac{-3\sqrt{2}}{80}, \frac{3\sqrt{2}}{160}, \frac{3\sqrt{2}}{160}, 0, \frac{-3\sqrt{2}}{80}, \frac{3\sqrt{2}}{160}, \frac{3\sqrt{2}}{160}, \frac{3\sqrt{2}}{80}, \frac{-3\sqrt{2}}{160}, \frac{-3\sqrt{2}}{160}, \frac{3\sqrt{2}}{80}, \frac{-3\sqrt{2}}{160}, \frac{-3\sqrt{2}}{160}, $$
$$\left. 0, \frac{\sqrt{2}}{240}, \frac{-\sqrt{2}}{480}, \frac{-\sqrt{2}}{480}, 0, \frac{\sqrt{2}}{240}, \frac{-\sqrt{2}}{480}, \frac{-\sqrt{2}}{480}, \frac{-\sqrt{2}}{240}, \frac{\sqrt{2}}{480}, \frac{\sqrt{2}}{480}, \frac{-\sqrt{2}}{240}, \frac{\sqrt{2}}{480}, \frac{\sqrt{2}}{480}\right\},$$

$$a_{\eta,j} = \left\{0, 0, \frac{-3\sqrt{6}}{32}, \frac{3\sqrt{6}}{32}, 0, 0, \frac{-3\sqrt{6}}{32}, \frac{3\sqrt{6}}{32}, 0, \frac{3\sqrt{6}}{32}, \frac{-3\sqrt{6}}{32}, 0, \frac{3\sqrt{6}}{32}, \frac{-3\sqrt{6}}{32}, \right.$$
$$0, 0, \frac{3\sqrt{6}}{160}, \frac{-3\sqrt{6}}{160}, 0, 0, \frac{3\sqrt{6}}{160}, \frac{-3\sqrt{6}}{160}, 0, \frac{-3\sqrt{6}}{160}, \frac{3\sqrt{6}}{160}, 0, \frac{-3\sqrt{6}}{160}, \frac{3\sqrt{6}}{160}, $$
$$\left. 0, 0, \frac{-\sqrt{6}}{480}, \frac{\sqrt{6}}{480}, 0, 0, \frac{-\sqrt{6}}{480}, \frac{\sqrt{6}}{480}, 0, \frac{\sqrt{6}}{480}, \frac{-\sqrt{6}}{480}, 0, \frac{\sqrt{6}}{480}, \frac{-\sqrt{6}}{480}\right\},$$

$$a_{\zeta,j} = \left\{ \frac{2475}{6416}, \frac{-2337}{12832}, \frac{-2337}{12832}, \frac{-2337}{12832}, \frac{-2475}{6416}, \frac{2337}{12832}, \frac{2337}{12832}, \frac{2337}{12832}, \frac{2337}{12832}, \frac{2337}{12832}, \frac{2337}{12832}, \frac{-2337}{12832}, \right.$$
$$\frac{-2337}{12832}, \frac{-2337}{12832}, \frac{-495}{6416}, \frac{2337}{64160}, \frac{2337}{64160}, \frac{2337}{64160}, \frac{495}{6416}, \frac{-2337}{64160}, \frac{-2337}{64160}, \frac{-2337}{64160}, \frac{-2337}{64160}, \frac{-2337}{64160},$$
$$\frac{-2337}{64160}, \frac{2337}{64160}, \frac{2337}{64160}, \frac{2337}{64160}, \frac{55}{6416}, \frac{-779}{192480}, \frac{-779}{192480}, \frac{-779}{192480}, \frac{-55}{6416}, \frac{779}{192480}, \frac{779}{192480}, \frac{779}{192480},$$
$$\left. \frac{779}{192480}, \frac{779}{192480}, \frac{779}{192480}, \frac{-779}{192480}, \frac{-779}{192480}, \frac{-779}{192480} \right\}.$$

The leading term of the isotropy error is given by

$$\epsilon = \frac{1}{81852120} \left(\frac{kL}{2}\right)^6 \left\{ 12813115 + 4071564\cos(4\vartheta) + 2449344\cos(6\vartheta) - 63495\cos(8\vartheta) \right.$$
$$\left. +512\cos(6\varphi)[10145 + 3729\cos(2\vartheta)]\sin(\vartheta)^6 \right\}. \tag{A.3}$$

The Jacobi-matrix for mapping the scheme to the physical grid is found to be

$$J = \begin{pmatrix} 1 & 0 & 0 \\ 0 & 1 & 0 \\ 0 & 0 & \frac{3208}{3987} \end{pmatrix}. \tag{A.4}$$

Appendix B. Six-block singularities

B.1. Second-order 20-point scheme

The coefficients are given by

$$a_{x,j} = \left\{ 0, 0, \frac{-263\sqrt{3}}{2520}, \frac{-263\sqrt{3}}{2520}, 0, \frac{263\sqrt{3}}{2520}, \frac{263\sqrt{3}}{2520}, 0, 0, \frac{-157\sqrt{3}}{5040}, \frac{-157\sqrt{3}}{5040}, 0, \frac{157\sqrt{3}}{5040}, \frac{157\sqrt{3}}{5040}, 0, \frac{-157\sqrt{3}}{5040}, \right.$$
$$\left. \frac{-157\sqrt{3}}{5040}, 0, \frac{157\sqrt{3}}{5040}, \frac{157\sqrt{3}}{5040} \right\}$$
$$a_{y,j} = \left\{ 0, \frac{263}{1260}, \frac{263}{2520}, \frac{-263}{2520}, \frac{-263}{1260}, \frac{-263}{2520}, \frac{263}{2520}, 0, \frac{157}{2520}, \frac{157}{5040}, \frac{-157}{5040}, \frac{-157}{2520}, \frac{-157}{5040}, \frac{157}{5040}, \frac{157}{2520}, \frac{157}{5040}, \right.$$
$$\left. \frac{-157}{5040}, \frac{-157}{2520}, \frac{-157}{5040}, \frac{157}{5040} \right\}$$
$$a_{z,j} = \left\{ \frac{61}{210}, 0, 0, 0, 0, 0, 0, \frac{-61}{210}, \frac{11}{315}, \frac{11}{315}, \frac{11}{315}, \frac{11}{315}, \frac{11}{315}, \frac{11}{315}, \frac{-11}{315}, \frac{-11}{315}, \frac{-11}{315}, \frac{-11}{315}, \frac{-11}{315}, \frac{-11}{315} \right\}.$$

The leading error term is found to be

$$\epsilon = \frac{1}{12} \left(\frac{kL}{2}\right)^2 [7 + \cos(2\vartheta)] + \mathrm{HOT}. \tag{B.1}$$

B.2. Fourth-order 16-point scheme

The coefficients are given by

$$a_{x,j} = \left\{ 0, 0, \frac{-2}{3\sqrt{3}}, \frac{-2}{3\sqrt{3}}, 0, \frac{2}{3\sqrt{3}}, \frac{2}{3\sqrt{3}}, 0, 0, 0, \frac{1}{12\sqrt{3}}, \frac{1}{12\sqrt{3}}, 0, \frac{-1}{12\sqrt{3}}, \frac{-1}{12\sqrt{3}}, 0 \right\}$$

$$a_{y,j} = \left\{0, \frac{4}{9}, \frac{2}{9}, \frac{-2}{9}, \frac{-4}{9}, \frac{-2}{9}, \frac{2}{9}, 0, 0, \frac{-1}{18}, \frac{-1}{36}, \frac{1}{36}, \frac{1}{18}, \frac{1}{36}, \frac{-1}{36}, 0\right\}$$

$$a_{z,j} = \left\{\frac{2}{3}, 0, 0, 0, 0, 0, 0, \frac{-2}{3}, \frac{-1}{12}, 0, 0, 0, 0, 0, 0, \frac{1}{12}\right\}.$$

The leading error of the ratio of numerical phase speed to true phase speed is given by

$$\epsilon = \frac{1}{480}\left(\frac{kL}{2}\right)^4 [130 + 45\cos(2\vartheta) + 78\cos(4\vartheta) + 3\cos(6\vartheta) - 16\cos(6\varphi)\sin(\vartheta)^6]. \tag{B.2}$$

B.3. Fourth-order 46-point scheme

The coefficients are given by

$$a_{x,j} = \left\{0, 0, \frac{-5}{6\sqrt{3}}, \frac{-5}{6\sqrt{3}}, 0, \frac{5}{6\sqrt{3}}, \frac{5}{6\sqrt{3}}, 0, 0, 0, 0, 0, 0, 0, 0, 0, 0, 0, 0, 0, 0, 0, 0, \frac{-1}{12\sqrt{3}}, \frac{-1}{12\sqrt{3}}, 0, \frac{1}{12\sqrt{3}}, \frac{1}{12\sqrt{3}}, 0,\right.$$
$$\left. 0, 0, 0, 0, 0, 0, 0, 0, 0, 0, 0, 0, \frac{1}{6\sqrt{3}}, \frac{1}{3\sqrt{3}}, \frac{1}{6\sqrt{3}}, \frac{-1}{6\sqrt{3}}, \frac{-1}{3\sqrt{3}}, \frac{-1}{6\sqrt{3}}\right\}$$

$$a_{y,j} = \left\{0, \frac{5}{9}, \frac{5}{18}, \frac{-5}{18}, \frac{-5}{9}, \frac{-5}{18}, \frac{5}{18}, 0, 0, 0, 0, 0, 0, 0, 0, 0, 0, 0, 0, 0, 0, \frac{1}{18}, \frac{1}{36}, \frac{-1}{36}, \frac{-1}{18}, \frac{-1}{36}, \frac{1}{36}, 0, 0, 0, 0, 0,\right.$$
$$\left. 0, 0, 0, 0, 0, 0, 0, 0, 0, \frac{-1}{6}, 0, \frac{1}{6}, \frac{1}{6}, 0, \frac{-1}{6}\right\}$$

$$a_{z,j} = \left\{\frac{2}{3}, 0, 0, 0, 0, 0, 0, 0, \frac{-2}{3}, 0, 0, 0, 0, 0, 0, 0, 0, 0, 0, 0, 0, 0, 0, \frac{-1}{12}, 0, 0, 0, 0, 0, 0, \frac{1}{12}, 0, 0, 0, 0, 0, 0, 0, 0, 0,\right.$$
$$\left. 0, 0, 0, 0, 0, 0, 0, 0, 0, 0\right\}.$$

The leading error of the phase speed is found to be

$$\epsilon = \frac{1}{960}\left(\frac{kL}{2}\right)^4 [210 + 165\cos(2\vartheta) + 126\cos(4\vartheta) + 11\cos(6\vartheta) + 128\cos(6\varphi)\sin(\vartheta)^6]. \tag{B.3}$$

References

[1] H.A. Grogger, Finite difference approximations of first derivatives for two-dimensional grid singularities, J. Comput. Phys. 217 (2) (2006) 642–657.
[2] A. Kumar, Isotropic finite-differences, J. Comput. Phys. 201 (1) (2004) 109–118.
[3] C.L. Wagner, J.B. Schneider, An acoustic finite-difference time-domain algorithm with isotropic dispersion, J. Comput. Acoust. 13 (2) (2005) 365–384.
[4] K.C. Chung, A generalized finite-difference method for heat transfer problems of irregular geometries, Numer. Heat Transfer 4 (1981) 345–357.
[5] C.K.W. Tam, J.C. Webb, Dispersion-relation-preserving finite difference schemes for computational acoustics, J. Comput. Phys. 107 (2) (1993) 262–281.
[6] C. Bogey, C. Bailly, A family of low dispersive and low dissipative explicit schemes for flow and noise computations, J. Comput. Phys. 194 (1) (2004) 194–214.
[7] S.K. Lele, Compact finite difference schemes with spectral-like resolution, J. Comput. Phys. 103 (1) (1992) 16–42.
[8] J.W. Kim, D.J. Lee, Optimized compact finite difference schemes with maximum resolution, AIAA J. 34 (5) (1996) 887–893.
[9] G. Ashcroft, X. Zhang, Optimized prefactored compact schemes, J. Comput. Phys. 190 (2) (2003) 459–477.
[10] J.A. Ekaterinaris, High-order accurate, low numerical diffusion methods for aerodynamics, Prog. Aerosp. Sci. 41 (2005) 192–300.
[11] R. Vichnevetsky, J. B. Bowles, Fourier analysis of numerical approximations of hyperbolic equations, SIAM Stud. Appl. Math. 1982.
[12] D.W. Zingg, H. Lomax, Finite-difference schemes on regular triangular grids, J. Comput. Phys. 108 (2) (1993) 306–313.
[13] R.D. Richtmyer, K.W. Morton, Difference Methods for Initial-Value Problems, Second ed., John Wiley & Sons, Inc., 1967.